Static and Dynamic Axial Response of Drilled Piers. II: Numerical Simulation

Gang Wang, M.ASCE[1]; and Nicholas Sitar, M.ASCE[2]

Abstract: Realistic time history simulation of drilled pier/pile-soil systems under dynamic and static loading is essential for the development of effective performance-based earthquake designs of deep foundations. This paper presents the results of the numerical simulation of a series of static and dynamic tests on drilled piers performed at the University of California, Berkeley. A nonlinear soil model was implemented based on multiaxial cyclic bounding-surface plasticity within a general finite-element framework, OpenSees. The model requires a small number of parameters that can be easily obtained through conventional site investigations. The results of the simulations show that the model can reasonably simulate nonlinear response of the soil and that it does a good job of capturing the actual load deformation curves obtained from in situ dynamic and static pier load tests. Although the model is suitable for a fully nonlinear total stress analysis of soil-pile systems under multidirectional shaking, further studies are needed to enhance the model capacity by incorporating the cyclic stiffness and strength degradation caused by full stress reversals. **DOI: 10.1061/(ASCE)GT.1943-5606.0000548.** © *2011 American Society of Civil Engineers.*

CE Database subject headings: Piers; Dynamic loads; Axial loads; Finite element method; Simulation; Deep foundations; Earthquake loads.

Author keywords: Drilled pier; Dynamic loading; Axial load; Finite-element analysis.

Introduction

A prototype static and dynamic axial load test program on drilled cast-in-place concrete piers performed on the campus of the University of California, Berkeley (Wang et al. 2011) provided an impetus for a numerical analysis of the results and for the development of a model capable of fully representing the observed behavior. This paper describes a nonlinear plasticity constitutive model that was implemented within the framework of the Open-Sees finite-element code to simulate the results of the test program. The objective was to develop a robust approach that would be suitable for predicting the expected behavior of pile foundations under a variety of static and dynamic loads. Because of the nonlinear transient nature of the soil-pile system and high computational requirements, to date, the application of nonlinear finite-element analysis to this problem has been limited. Therefore, an important objective of the work presented in this paper was to develop a soil model simple enough to be computationally efficient, yet able to capture the cyclic stress-strain behavior (i.e., the modulus degradation and energy dissipation during cyclic loading). In addition, the model should have the potential to be used in three-dimensional site response and soil-structure interaction analysis. This paper presents a nonlinear soil model implementation based on multiaxial cyclic bounding-surface plasticity, and its validation through simulation of field tests on prototype drilled piers subjected to static and dynamic axial loading.

Constitutive Model for Cyclic Soil Response

Although there are many candidates for approaching the problem, models based on the concept of nested yield surfaces provide great flexibility when modeling cyclic soil response (Prevost 1977, 1985). By incorporating a phase-transformation surface that delimitates phases of contraction and dilation, the models can also be further extended to analyze the cyclic mobility of the sand and postliquefaction site response (Elgamal et al. 2002, 2003). However, nested yield surface models approximate nonlinear soil behavior in a discrete sense and require significant computer storage for robust numerical implementation. Motivated by the need for a smooth evolution of nonlinearity, Borja and Amies (1994) proposed a bounding-surface plasticity model, called the multiaxial cyclic plasticity model, for cyclic clay behavior. Because of its simplicity, the multiaxial cyclic plasticity model can be effectively used in a numerical procedure such as the finite-element scheme. Borja and his coworkers used this type of model for three-dimensional finite-element analysis of the vibration of undrained clay foundations (Borja and Wu 1994), for the nonlinear site response of Lotung LSST during the Taiwan earthquake of 20 May, 1986 (Borja et al. 1999a, b), and for the nonlinear site response of the Gilroy 2 reference site during the Loma Prieta earthquake of 17 October 1989 (Borja et al. 2000). This model was also successfully used to characterize nonlinear site-specific response under near-fault ground motions (Rodriguez-Marek 2000). These previous studies have demonstrated the success of the model in modeling site-specific response and the model's numerical stability. However, this type of model has not been used in the analysis of a strongly kinematically coupled problem, such as the pile-structure system. The mobilized maximum shear strain of soils in the Lotung site analysis was only approximately 0.2%, and the model has not been used for large strains.

[1]Assistant Professor, Dept. of Civil and Environmental Engineering, Hong Kong Univ. of Science and Technology, Clearwater Bay, Kowloon, Hong Kong (corresponding author). E-mail: gwang@ust.hk

[2]Professor, Dept. of Civil and Environmental Engineering, Univ. of California, Berkeley, CA 94720.

The basic concept of bounding-surface plasticity is that no purely elastic region exists in the stress-strain relationship; instead, the nonlinearity of the soil is modeled by smoothly transforming the tangential shear modulus from a small-strain modulus to a full plastic state through a state-dependent hardening modulus. A stress function called bounding surface ($\mathcal{B}$) is used to specify the full plastic state

$$\mathcal{B} = \|\hat{\boldsymbol{\sigma}}' - \beta\| - R = 0 \tag{1}$$

where $\hat{\boldsymbol{\sigma}}'$ = stress image point; β = deviatoric back stress of bounding surface; and R = radius of bounding surface. Prime ($'$) is used exclusively to signify that a tensor is deviatoric. The stress image point is located on the bounding surface and is projected from the current stress point $\boldsymbol{\sigma}'$ and the last stress reversal point $\boldsymbol{\sigma}_0'$ [Fig. 1(a)]. The radius of the bounding surface R can be related to the undrained shear strength S_u through the following relationship:

$$R = \sqrt{\frac{8}{3}} S_u \tag{2}$$

For clays under undrained conditions, the bounding surface is assumed to be pressure-independent and is circular if viewed in the deviatoric stress plane (π-plane). The rate form of the constitutive relationship can be written as

$$\dot{\boldsymbol{\sigma}}' = 2G\dot{\varepsilon}' = 2G_{\max}\left(1 + \frac{3G_{\max}}{H'}\right)^{-1}\dot{\varepsilon}' \tag{3}$$

where $\boldsymbol{\sigma}'$ = deviatoric stress and ε' = deviatoric strain, with prime used here to denote that they are deviatoric tensors. G = tangential shear modulus; $G_{\max}$ = maximum-shear modulus at small strains,

and H' = hardening modulus depending on the position of the current stress point.

The development of nonlinearity is manifested in the evolution of hardening modulus H' and shear modulus G. Among many interpolation schemes, the radial mapping rule is most widely used in the bounding-surface plasticity, in that the hardening modulus depends on the radial position of the current stress point. Given a most-recent stress reversal point $\boldsymbol{\sigma}_0'$, the current deviatoric stress $\boldsymbol{\sigma}'$, and its image point $\hat{\boldsymbol{\sigma}}'$ on the bounding surface $\mathcal{B}$ [see Fig. 1(a)] a dimensionless scalar κ can be defined to measure the relative distance of these stress points

$$\kappa = \frac{\|\hat{\boldsymbol{\sigma}}' - \boldsymbol{\sigma}'\|}{\|\boldsymbol{\sigma}' - \boldsymbol{\sigma}_0'\|} \tag{4}$$

Accordingly, the hardening modulus H' is determined through a smooth function of κ. One example of such a function can be chosen as the exponential form, as follows:

$$H' = h\kappa^m + H_0 \tag{5}$$

in which h = modulus parameter; m = dimensionless scalar; and H_0 = the kinematic hardening modulus for translation of the bounding surface in the stress space. Contours of constant H', named contour surface $\mathcal{F}$, are also circular in the π-plane, as shown in Fig. 1(a). Using Eq. (3), the soil behaves as instantaneously elastic around the stress reversal point (i.e., $H' \to \infty$ and $G \to G_{\max}$ as $\boldsymbol{\sigma}' \to \boldsymbol{\sigma}_0'$) and transits asymptotically toward the fully plastic stage on the bounding surface (where $H' = H_0$). The exponential parameters h and m control the rate of shear modulus degradation, and they can be determined by curve fitting the measured modulus-degradation curve.

(a) Bounding surface mapping rule

(b) Loading/unloading criterion

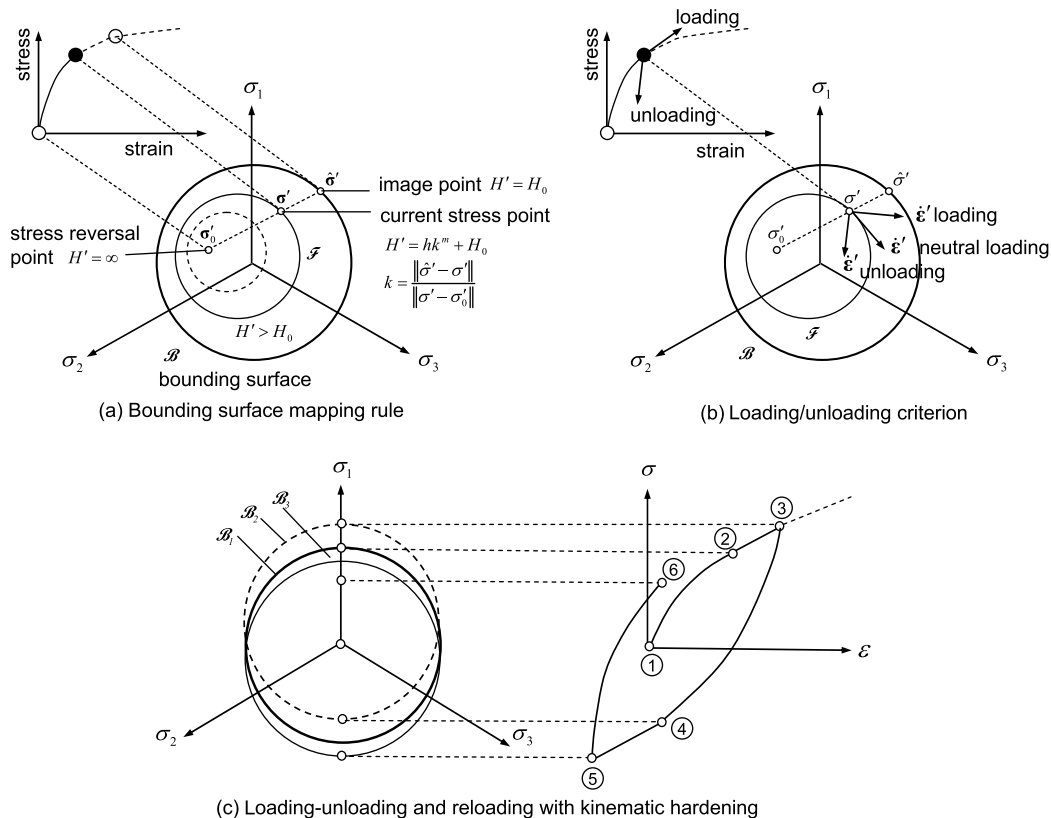(c) Loading-unloading and reloading with kinematic hardening

Fig. 1. Cyclic soil model, adapted from Borja and Amies (1994) and Borja et al. (1999a)

Identification of loading/unloading is critical for the cyclic material model. According to Borja and Amies (1994), the unloading condition can be interpreted as the instant the hardening modulus increases (i.e., $H' > 0$), which is equivalent to the following statement:

$$\chi = \frac{(1+\kappa)(\boldsymbol{\sigma}' - \beta) + \kappa(1+\kappa)(\boldsymbol{\sigma}' - \boldsymbol{\sigma}'_0)}{(\boldsymbol{\sigma}' - \beta):(\boldsymbol{\sigma}' - \boldsymbol{\sigma}'_0) + k(\boldsymbol{\sigma}' - \boldsymbol{\sigma}'_0):(\boldsymbol{\sigma}' - \boldsymbol{\sigma}'_0)} : \dot{\varepsilon}' < 0 \quad (6)$$

Wang and Sitar (2006) further simplified the preceding equation and provided a new loading/unloading criterion expressed by the inner product (double contraction) of the strain increment $\dot{\varepsilon}'$ and the out normal tensor $\mathbf{n}$ of $\mathcal{F}$, as follows:

$$\chi = \mathbf{n}:\dot{\varepsilon}' \begin{cases} > 0, & \text{loading} \\ = 0, & \text{neutral loading} \\ < 0, & \text{unloading} \end{cases} \quad (7)$$

The preceding expression is equivalent to Eq. (6), but it has straightforward geometrical interpretation. The loading/unloading criterion can be stated as follows: the soil is undergoing loading if the deviatoric strain increment $\dot{\varepsilon}'$ points outward from the contour surface $\mathcal{F}$; is unloading if $\dot{\varepsilon}'$ points inward; and is neutral-loading if $\dot{\varepsilon}'$ is tangential to $\mathcal{F}$. The criterion is also illustrated in Fig. 1(b) for this geometrical interpretation. Compared with Eq. (6), the new criterion in Eq. (7) is more intuitive and is similar to the loading/unloading condition in the classical theory of plasticity.

Once the unloading is identified, all previous $\mathcal{F}$ surfaces dissolve. Stress reversal point $\boldsymbol{\sigma}'_0$ is updated to the new stress unloading point (which coincides with $\boldsymbol{\sigma}'$ on just unloading), and new $\mathcal{F}$ surfaces for constant hardening modulus H' are recentered around the new position to interpolate the subsequent loading process. Fig. 1(c) schematically illustrates a cyclic soil response simulated by the model. Starting from the initial stress point 1, the nonlinear stress-strain curve from 1 to 2 is governed by the bounding-surface hardening law. The shear modulus smoothly degenerates from the maximum value at point 1 to a constant residual value at point 2, where the stress point hits the bounding surface $\mathcal{B}_1$. The full plastic stage is reached from point 2 to 3, and the bounding surface hardens kinematically from $\mathcal{B}_1$ to $\mathcal{B}_2$. Once the unloading condition is detected at point 3, the stress reversal point is updated to that point, and a new interpolated nonlinear stress-strain relationship is developed until the stress point reaches the bounding surface again at point 4. After $\mathcal{B}_2$ hardens to $\mathcal{B}_3$, i.e., from point 4 to point 5, the soil is reloaded to point 6.

To be implemented in a numerical analysis program, the rate constitutive equation of the nonlinear material model needs to be numerically integrated. The algorithmic consistent tangent is derived from the exact linearization of the discrete constitutive relationship, and it is usually needed to improve the stability and efficiency of the global solution scheme. As pointed out by Simo and Taylor (1985), the use of the algorithmic consistent tangent is essential to preserve the asymptotic global quadratic rate of convergence of the Newton-Raphson scheme, whereas using the continuum tangent may deteriorate the rate of convergence. Detailed algorithmic derivation for this model is presented in Wang and Sitar (2006).

Determination of Model Parameters

Table 1 summarizes recommended methods to determine model parameters. The maximum shear modulus at small strain, $G_{\max}$, can be computed from the shear-wave velocity profile

Table 1. Determination of Model Parameters

Model parameters		Calibration methods
Elastic Parameters	$G_{\max}$	From shear-wave velocity profile, $G_{\max} = \rho V_s^2$
	ν	Poisson's ratio
Strength parameter	S_u	From unconfined compression test or SPT correlation
Hardening parameters	h, m	Shear-modulus-reduction curves
	H_0	Tangential shear modulus at large strains

$$G_{\max} = \rho V_s^2 \quad (8)$$

where ρ = soil density and V_s = measured shear-wave velocity of the soil. The undrained shear strength, S_u, which determines the radius of the bounding surface R [see Eq. (2)] can be determined from unconfined compression (UC) test or from empirical correlation such as standard penetration test (SPT) data.

As described previously, the nonlinear stress-strain relationship within the bounding surface is governed by the exponential hardening law. The two hardening parameters h and m control the rate of modulus degradation. Fig. 2 presents a cyclic simple-shear response produced by a strain-controlled single finite-element test. The soil element is assumed to have maximum shear modulus $G_{\max} = 1.67 \times 10^5$ kPa, which corresponds to a typical stiff clayey soil with a density of 2×10^3 kg/m^3 and a shear-wave velocity of 289 m/s. Poisson's ratio is assumed as $v = 0.49$ and the undrained shear strength determined from unconfined compressive strength test is assumed as $S_u = 100$ kPa. The hardening modulus for the bounding surface is assumed to be zero ($H_0 = 0$). As shown in Fig. 2(a), for a given $m = 0.8$, a larger h predicts a more elastic cyclic response. As a limit case, the perfectly elastoplastic J_2 response can be approximated by using a large h value ($h \geq 10$ in this case). Fig. 2(b) gives predicted cyclic loops for a given $h = 0.7G_{\max}$ and a varying m from 0.8 to 2.0. The stress-strain relationship for a larger m is more elastic right on stress reversal; however, the curve bends over more quickly at a high stress level. Because a very small tangential modulus has been developed well before the stress point reaches the bounding surface, the soil apparently yields at a lower stress level for the case of larger m. Fig. 2(c) plots cyclic stress-strain curves with increasing magnitude of control strains. The Masing rule is well approximated by the cyclic curves. Note that for a single cycle, a closed loop is not immediately formed. Instead, slight strength degradation is captured naturally by the model [Fig. 2(d)].

The cyclic stress-strain responses can also be represented in the form of a modulus-reduction curve. The modulus-reduction curve plots the ratio of secant-shear modulus and maximum-shear modulus versus shear strains applied. As presented in Fig. 3, variations in h and m result in a family of modulus-reduction curves. Modulus-reduction curves for clays [plasticity index (PI) values of 0, 15, and 30 in dashed lines, left to right] from Vucetic and Dobry (1991) are also illustrated for comparison. Although increases in h and m both shift modulus-reduction curves to the right of the strain axis, their ranges of influence are different: variation in h affects the curve shape over small to large strain ranges (10^{-4} to 1%), whereas variation in m primarily changes curve shape over small to medium strain levels (10^{-4} to 10^{-1}%). The suitable combination of h and m can be determined by fitting two points on a measured modulus-degradation curve, so that the parameters can be related to fundamental properties of the soil. The hardening modulus of the bounding surface, H_0, can be determined by fitting the tangential shear-modulus at large strains.
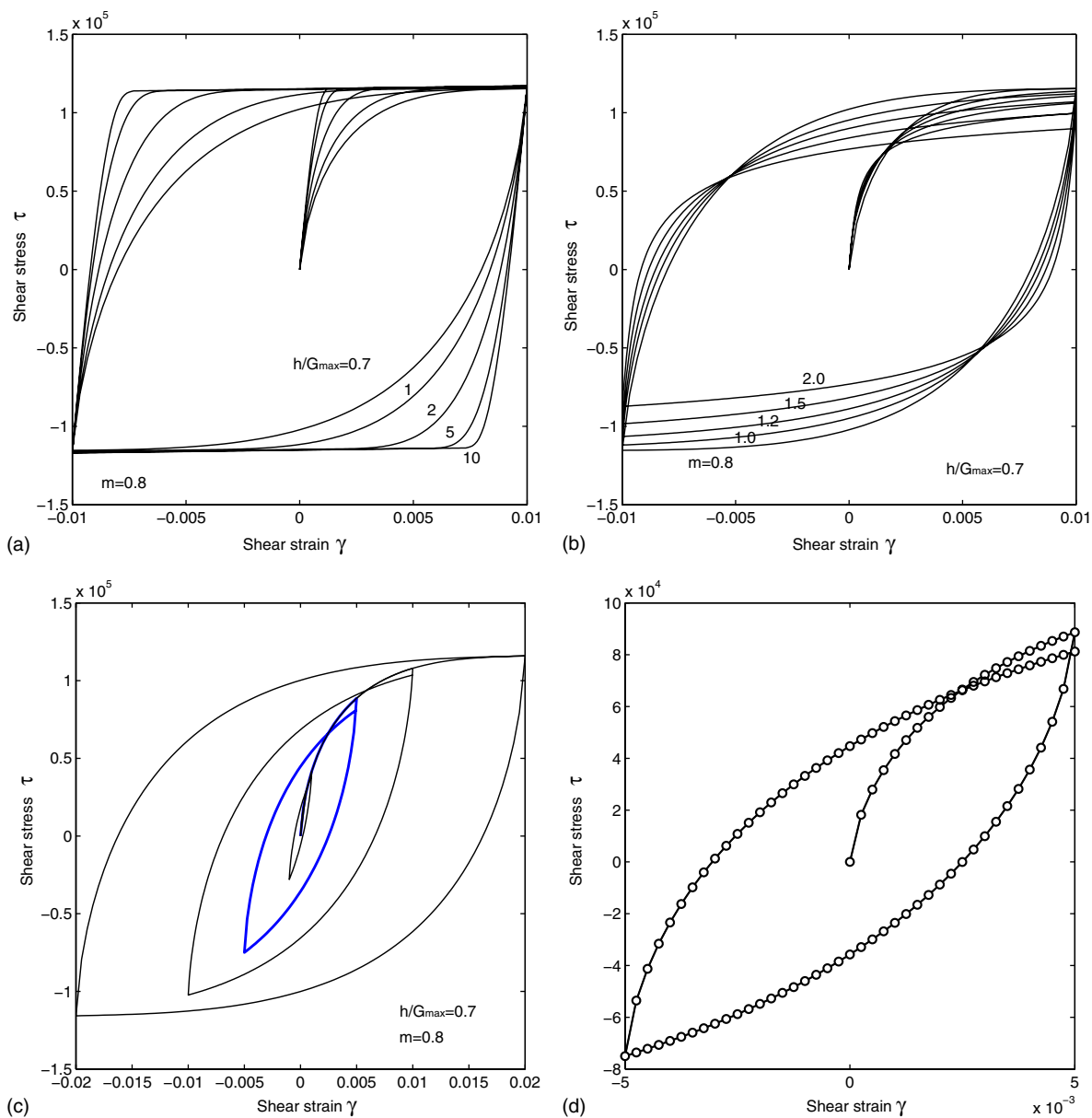
Fig. 2. Computed cyclic simple shear response

In summary, the bounding-surface cyclic soil model has analytical features that can simulate three-dimensional nonlinear cyclic soil response quite realistically, and it can capture most important aspects of dynamic simulation, namely, modulus reduction and hysteretic energy dissipation. Furthermore, the model requires minimal parameters that can be easily calibrated from data obtained through a conventional field investigation.

Simulation of the Axial Pier Response

The preceding constitutive relationship was implemented in the OpenSees (OpenSees Version 2.3.2) finite-element framework to simulate a series of full-scale load tests on drilled piers. The details of the drilled pier design, installation, and load test protocol are presented in Part I of this paper (Wang et al. 2011). To summarize, the test site is located south of the University of California, Berkeley campus, and is primarily underlain by hard to very stiff sandy clay, medium-dense sandy silt, and dense clayey sand.

All test piers were cast-in-place concrete piers, with dimensions of 6–9 m (20–30 ft) long and 61–76 cm (2–2.5 ft) in diameter. A sequence of dynamic impacts, designed to be approximately 200–400 ms each in duration, was applied on the pier head. After the dynamic pile load test (PLT), static tension or compression tests were also performed to evaluate the effect of loading rate.

The Finite-Element Model

The cyclic soil model can be easily implemented in a nonlinear finite-element framework, such as OpenSees. First, the numerical results of simulations of the test on Pier A1-19 are presented. The pier is 5.8 m (19 ft) long and 0.76 m (2.5 ft) in diameter. Water level was encountered at a depth of 6.1 m (20 ft). The pier was first loaded dynamically using the PLT device, and the dynamic test was followed by a static compression test (Wang et al. 2011). Because of the symmetry of the problem, only one-half of the soil-pier cross section was meshed by using the axisymmetric bilinear
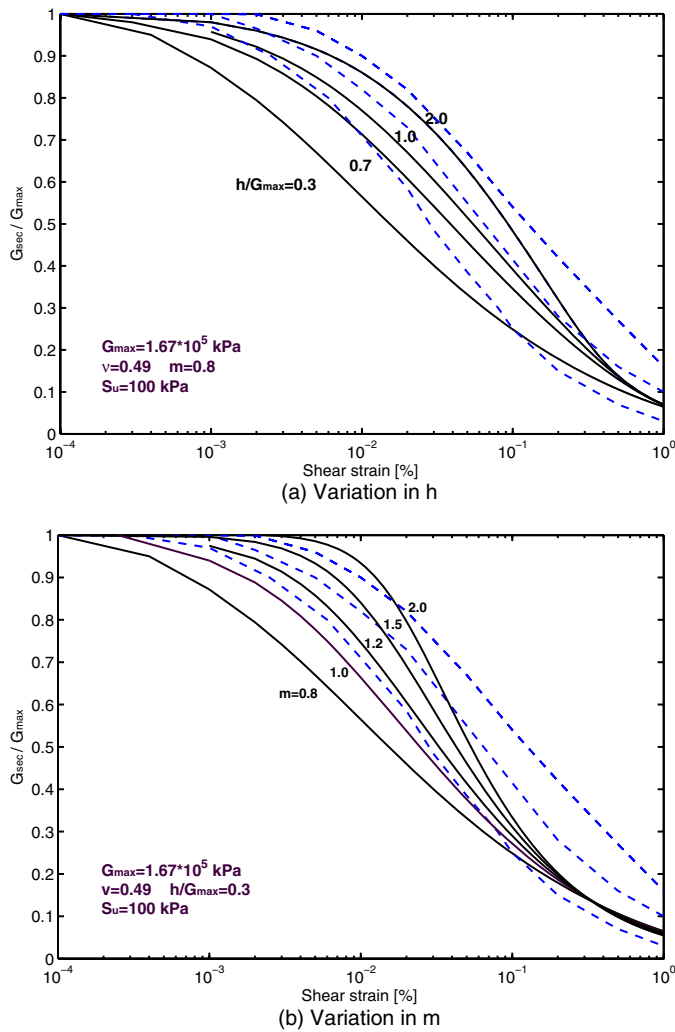
Fig. 3. Computed modulus-reduction curves; dashed lines are for PI values of 0, 15, and 30, from Vucetic and Dobry (1991)

Fig. 4. An example of finite-element mesh

element. The finite-element mesh, shown in Fig. 4, extended to 18.3 m (60 ft) in depth and 18.3 m (60 ft) in length, with 123 elements for the pier and 11,446 elements for the soils. The nodes along the base were fixed to represent the rock layer at that depth. For dynamic analysis, transmitting boundary elements were prescribed along the right side of the domain to transmit outcoming waves through the domain boundary and minimize the reflected waves.

Traditionally, frictional contact can be placed along the pier-soil interface to allow for slippage between pairs of pier and soil elements. However, field observations revealed that the failure surface of cast-in-place concrete piers did not occur exactly on the material interface, but some distance into the surrounding soil. Instead of utilizing artificial contact elements, the pier and soil elements were assumed perfectly bonded in the analysis. Interface behavior was modeled as plastic yielding through nonlinear soil elements adjacent to the pier shaft. Very fine mesh was used in that region, as shown in Fig. 4(b). A mesh-sensitive study was performed to investigate the effects of element size on the simulated results. The study showed that the vertical soil displacement was primarily concentrated within one-half of the pier radius distance away from the pier wall. Refining the soil elements within that region may lead to a converged displacement profile. Compared to an "exact" solution obtained by using a superfine mesh, the mesh used in the analysis
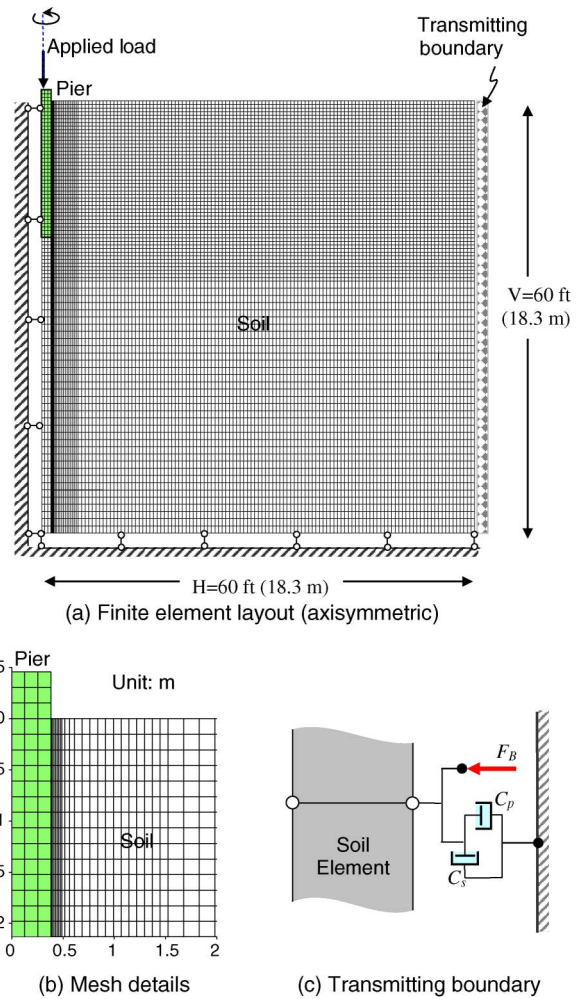
was fine enough and yielded a less than 0.4% relative error in the displacement solution.

It was important for the ensuing analysis that the initial in situ stress state be properly developed. A staged loading process was designed to enforce the in situ stress state of the soil elements: The soil elements were initially assumed to be linearly elastic, with Poisson's ratio determined by $v = K_0/(1 + K_0)$, where K_0 is the coefficient of earth pressure (approximately 0.5 for normally consolidated clays). After vertical consolidation under self-weight to generate the desired K_0 profile, the soil elements were allowed to behave nonlinearly.

The transmitting boundary is illustrated in Fig. 4(c). For each transmitting element, two dashpots were placed parallel and normal to the boundary to absorb the shear wave and the pressure wave. By imposing equivalent viscous forces to the soil nodes, the transmitting elements simulated the truncated half-space to minimize the wave reflection (see Lysmer and Kuhlemeyer 1969; Deeks and Randoloph 1994). The damping constant of the dashpot per unit area was determined as

$$C_s = \rho_{\text{soil}} V_s \quad \text{and} \quad C_p = \rho_{\text{soil}} V_p \qquad (9)$$

where ρ_{soil} = soil density and V_s and V_p = s-wave velocity and p-wave velocity in the soil, respectively. The in situ lateral force obtained from the self-weight consolidation, F_B, was also applied to the soil node along the boundary to maintain its static force equilibrium. The performance of the transmitting boundary was

compared with an "exact" solution obtained by using an extended finite-element mesh, in which the pier response was not affected by the boundary condition. The transmitting boundary effectively dissipated the outcoming wave, and the solution was almost identical to the "exact" solution.

To model incompressible material behavior, such as undrained clays, axisymmetric *B*-bar formulation was implemented in the finite-element interpolation to avoid the volumetric locking phenomenon at the incompressibility limit (see Zienkiewicz and Taylor 2000). The essence of the *B*-bar formulation is modifying the terms associated with volumetric strain in the element, so that incompressibility is satisfied in a volume average sense.

In the dynamic finite-element analyses, very small viscous damping was also used for the purpose of stabilizing the numerical results. Stiffness-proportional Rayleigh damping was used, in which the viscous damping matrix $[\mathbf{C}]$ is related to the mass matrix $[\mathbf{M}]$ and initial stiffness matrix $[\mathbf{K}]$ as

$$[\mathbf{C}] = \alpha[\mathbf{M}] + \beta[\mathbf{K}] \qquad (10)$$

The formulation produces a frequency-dependent damping ratio ξ in the system if the harmonic input wave has an angular frequency ω

$$\xi = \frac{1}{2}\left(\frac{\alpha}{\omega} + \beta\omega\right) \qquad (11)$$

By setting the mass-proportional coefficient $\alpha = 0$, the stiffness-proportional coefficient β can be determined from the following relationship:

$$\beta = \frac{2\xi}{\omega} = \frac{\xi T}{\pi} \qquad (12)$$

where T is the period of the input motion.

A value of $\beta = 0.0003$ was used in the dynamic simulation, which represented a viscous-damping ratio of $\xi < 1\%$ if the wave period is longer than 0.1 s. Note that the duration of each dynamic

pier load cycle is around 0.2–0.3 s. Therefore, soil damping is primarily provided through frequency-independent hysteretic damping, and the viscous damping is very small and is used only to regulate the numerical instability.

The choice of time step in nonlinear dynamic analyses must satisfy both the numerical stability and the numerical accuracy requirement. Guidelines for choosing the time step for linear and nonlinear dynamic analyses can be found in Bathe (1996) and Hughes (1987). A dissipassive Newmark algorithm was used for time integration, and a Newton-Raphson scheme was used to solve the global system. Because the adopted Newmark algorithm is implicit and unconditionally stable, the choice of the time step is primarily based on obtaining acceptable numerical accuracy. Although no theoretical solution exists to quantify the integration errors of a complex system, sufficiently accurate results ($< 1\%$ error in amplitude decay and period elongation) can be achieved for a linear system of hyperbolic partial differential equations if $\Delta t/T < 0.02$, where T = period of input harmonic motion (Bathe 1996). Therefore, $\Delta t = 0.005$ s (i.e., $\Delta t/T < 0.02$) was used in the dynamic analysis, so that the numerical accuracy could be satisfied. Moreover, cases were tested using a smaller time step $\Delta t = 0.001$ s, and the relative error in calculated total displacement was less than 0.5%.

Model Parameters for Static and Dynamic Analyses

The concrete pier was assumed to be linearly elastic, because stress developed during the test was well below the tensile and compressive strength of the concrete. The elastic modulus of the concrete pier was assumed to be 20 GPa, with Poisson's ratio $v = 0.1$ and density 2.4×10^3 kg/m^3 (150 pcf). On the basis of the sample test from the site, the soil density was measured as $\rho = 2 \times 10^3$ kg/m^3 and Possion's ratio $v = 0.4$. Spectral analysis of surface waves (SASW) measured the shear-wave velocity profile, shown in Fig. 5(a). The average shear velocity over the pier length was
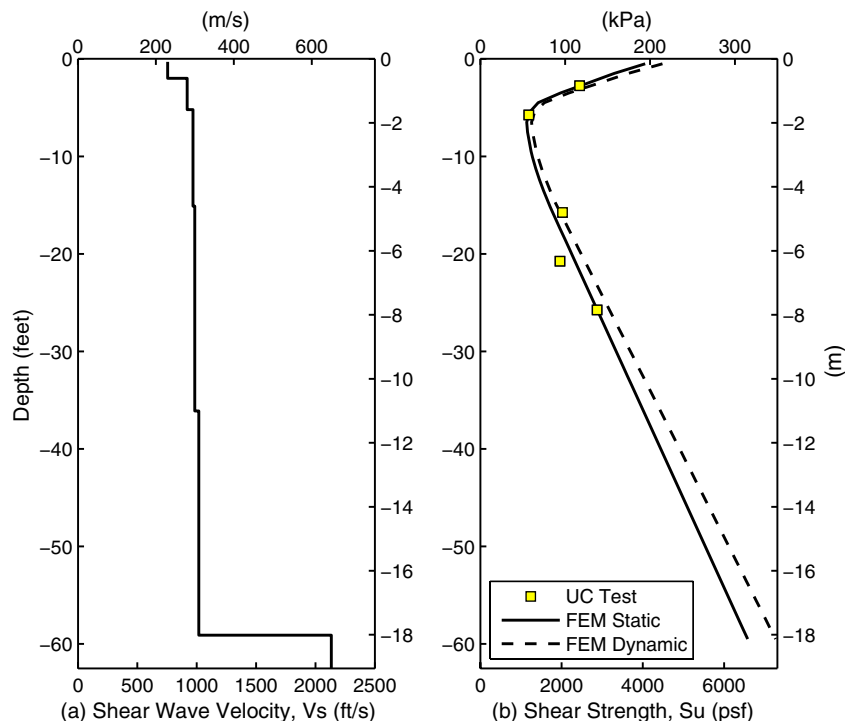

Fig. 5. Profiles of soil parameters

$V_s = 289$ m/s, so the small strain shear modulus $G_{max} = \rho V_s^2$ was computed using this value. The undrained shear strength (S_u) profile was estimated from an unconfined compression (UC) test, as shown in Fig. 5(b). The shear-strength profile shows fairly high strength in the soil close to the surface, indicating that the soil is overly consolidated at the top. The high overconsolidation ratio (OCR) may be attributed to desiccation and unloading of overburden pressure during deep excavation when the test site was constructed. To account for the loading rate effect, the S_u profile used in the dynamic case was chosen to be slightly higher than the static case.

During a PLT, a dynamic load $F(t)$ was applied on the top of the test pier. A typical load history measured during the test of a single-load cycle (Fig. 6) can be reasonably approximated by a trigonometric function as

Fig. 6. Approximated PLT cyclic load

$$F(t) = \frac{P}{4}\left[1 - \cos\left(\frac{2\pi t}{T}\right)\right]^2 \tag{13}$$

where P and T = magnitude and duration of the load pulse. During the analysis, load pulses were repeatedly applied on the top of the pier, with magnitude P for each pulse assumed as the value of actual measurement, and T assumed to be 0.3 s for all pulses. The vertical movements of all top surface nodes of the pier were constrained to move identically.

The soil-modulus reduction and damping factors during cyclic loadings depend on a number of factors, including the amplitude of cyclic strain developed in the soil, PI, void ratio, OCR, confining pressure, frequency, and shape of the cyclic loading-time history (Seed et al. 1984; Sun et al. 1988; Vucetic et al. 1998a, b). For cohesive soils, the PI has an important influence on the modulus-reduction curves (Vucetic and Dobry 1991). With increasing shear strain, clays with higher plasticity indexes tend to behave more elastically than low-PI soils, resulting in a slower rate of modulus reduction and a lower damping ratio. Similarly, the modulus of sands reduces much faster than that of clays, and the damping ratio for sands is generally larger. Recent experimental investigations also reveal significant dependence of the form of the modulus-reduction curve on the applied strain rate (Matešić and Vucetic 2003; Vucetic and Tabata 2003). It is recognized that the rate effect on the stiffness and strength of the soil can be attributed to the viscosity in the soil skeleton and the associated creeping, stress relaxation process. Because of the rate effect, dynamic and static modulus-reduction curves can be quite distinctive, especially at small strains. This issue has been examined in comparisons of monotonic and cyclic laboratory tests at varying strain rates (LoPresti et al. 1996; Shibuya et al. 1996). On the basis of the experiments, the maximum modulus at small strains is not significantly influenced by the imposed strain rate. On the other hand, the elastic
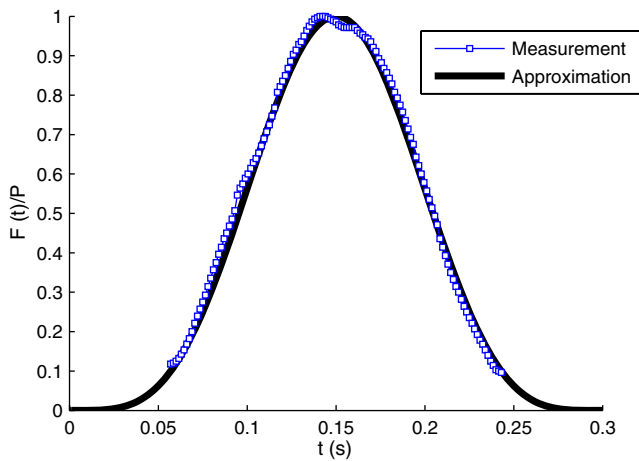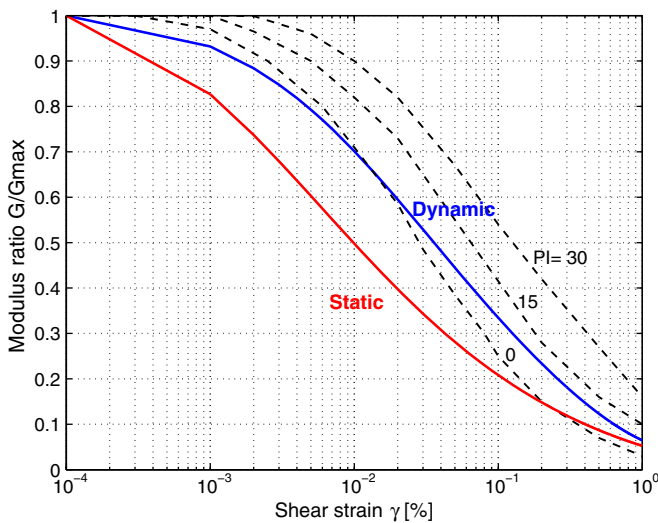

Fig. 7. Modulus-reduction curves

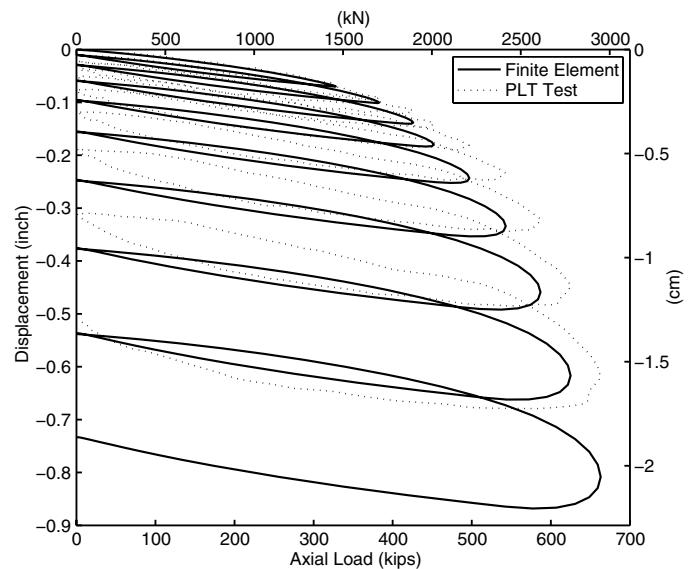**Fig. 8.** Finite-element simulation of PLT on Pier A1-19

Table 2. Soil Parameters Used in Dynamic and Static Analysis

	ρ	ν	G_{max}	S_u	h	m	H_0
Dynamic	2×10^3 kg/m^3	0.4 for unsaturated;	1.67×10^5 kPa	Profile in Fig. 5	0.70 G_{max}	0.8	$G_{max}/300$
Static		0.49 for saturated			0.25 G_{max}		

threshold strain is influenced by the strain rate, increasing with the increasing strain rate. Beyond the elastic threshold strain, the moduli degrade at a much faster rate under monotonic loading than under dynamic loading. The effect of loading rate also varies with the soil type. In general, the rate effect is very small in clean sands and nonplastic silts, relatively small in silty and clayey sands, and significant in clayey soils (Matešić and Vucetic 2003). Moreover, the strain rate effect in clays generally increases with the PI and water content.

Because the shear-modulus-reduction curve is rate-dependent, the effect has significant implications on the numerical modeling procedure. In general, the rate effect can be taken into account in two ways. One is to develop a rate-dependent constitutive model for the soil, so that the rate effect can be simulated by the model. This scheme is appealing because it can accommodate variation in the strain rate during a loading history, but is unfortunately limited in its practical use. The second approach, used in this paper, considers different soil parameters for the static case and dynamic case,

so that the dependence of soil parameters on the strain rate can be considered explicitly.

As described previously, two hardening parameters, h and m, are used to adjust the shape of the cyclic curves. They can be fitted to the modulus-reduction curve of various soil types. On the basis of the site information, the hardening parameters h and m are chosen to fit the low-PI range of Vucetic and Dobry curves in the dynamic simulation (Vucetic and Dobry 1991). For the static analysis, we calculated a static modulus-reduction curve, which degrades faster than the dynamic curve. The difference is consistent with that observed in the laboratory tests. The modulus-reduction curves used in the analyses are shown in Fig. 7, with the Vucetic and Dobry curves for PI values of 0, 15, and 30 shown in dashed lines. Table 2 summarizes the soil parameters used for dynamic and static analyses. The dynamic and static analyses used similar parameters, except that the hardening parameter $h = 0.70 \ G_{max}$ was assigned for the dynamic case and $h = 0.25 \ G_{max}$ for the static case. Other hardening parameters ($m = 0.8$, $H_0 = G_{max}/300$) were used for both cases.
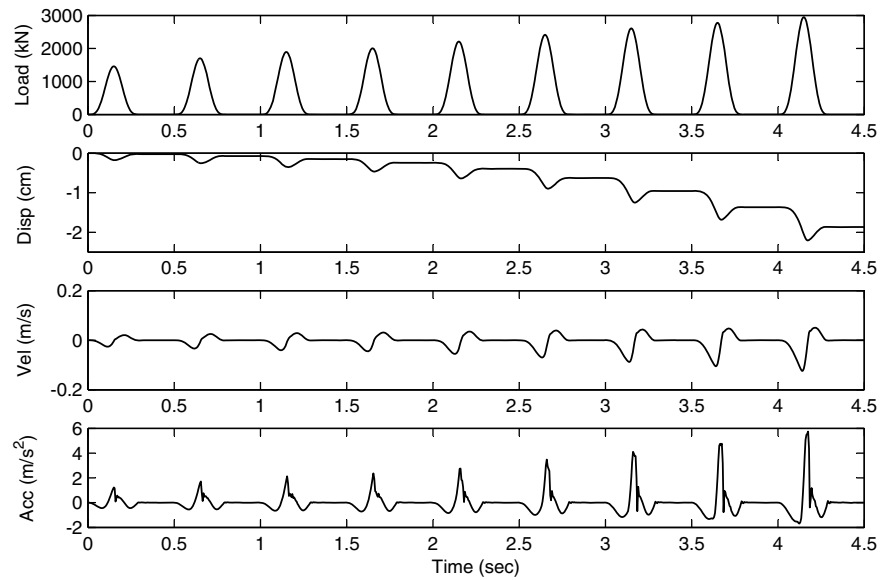

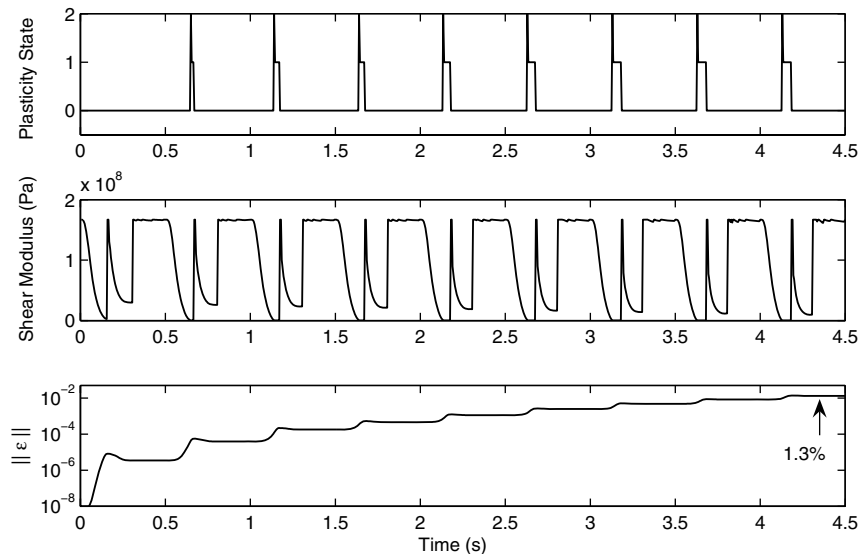**Fig. 9.** Computed pier head reaction under the complete PLT load sequence

Fig. 10. Typical nonlinear response for a soil element along pier-soil interface

Simulation of Dynamic PLTs

Fig. 8 shows the recorded (dashed lines) and predicted (solid lines) PLT curves for Pier A1-19 head displacement versus the applied load history. The plot shows that the dynamic soil-pier stiffness for loading and unloading, as well as residual displacements and energy dissipation for all nine load cycles, can be simulated reasonably well. The overall strength envelope, which encompasses all these loops, closely follows the actual measurement. During the test, there was considerable rebound at the end of each load cycle, which cannot be adequately simulated. The lack of rebound accumulates to produce the apparently larger predicted total residual displacement (1.8 cm predicted against 1.3 cm measured).

Fig. 9 further juxtaposes typical displacement, velocity, and acceleration time histories of the top node in reaction to the applied load. When the load increases, the pier accelerates downward, accumulating velocity and displacement. Displacement achieves its maximum value at the point when velocity passes through zero, and reduces afterward. It is evident that the peak displacement lags slightly behind the peak load point because of the inertial effect. A similar pattern is repeated when increasing magnitude of the cyclic peak load is applied. In the last two load cycles, the downward peak velocity reaches 0.1 m/s and the acceleration reaches 2 m/s² downward and 6 m/s² upward.

A detailed response of a nonlinear soil element adjacent to the pile wall is presented in Fig. 10. With the increasing load, the element experiences loading from its initial stress state, and its shear modulus degrades from its maximum value (small-strain modulus) to the current value according to the bounding-surface mapping rule. Upon stress unloading, the current stress state is set as the new unloading point, and the shear modulus is set back
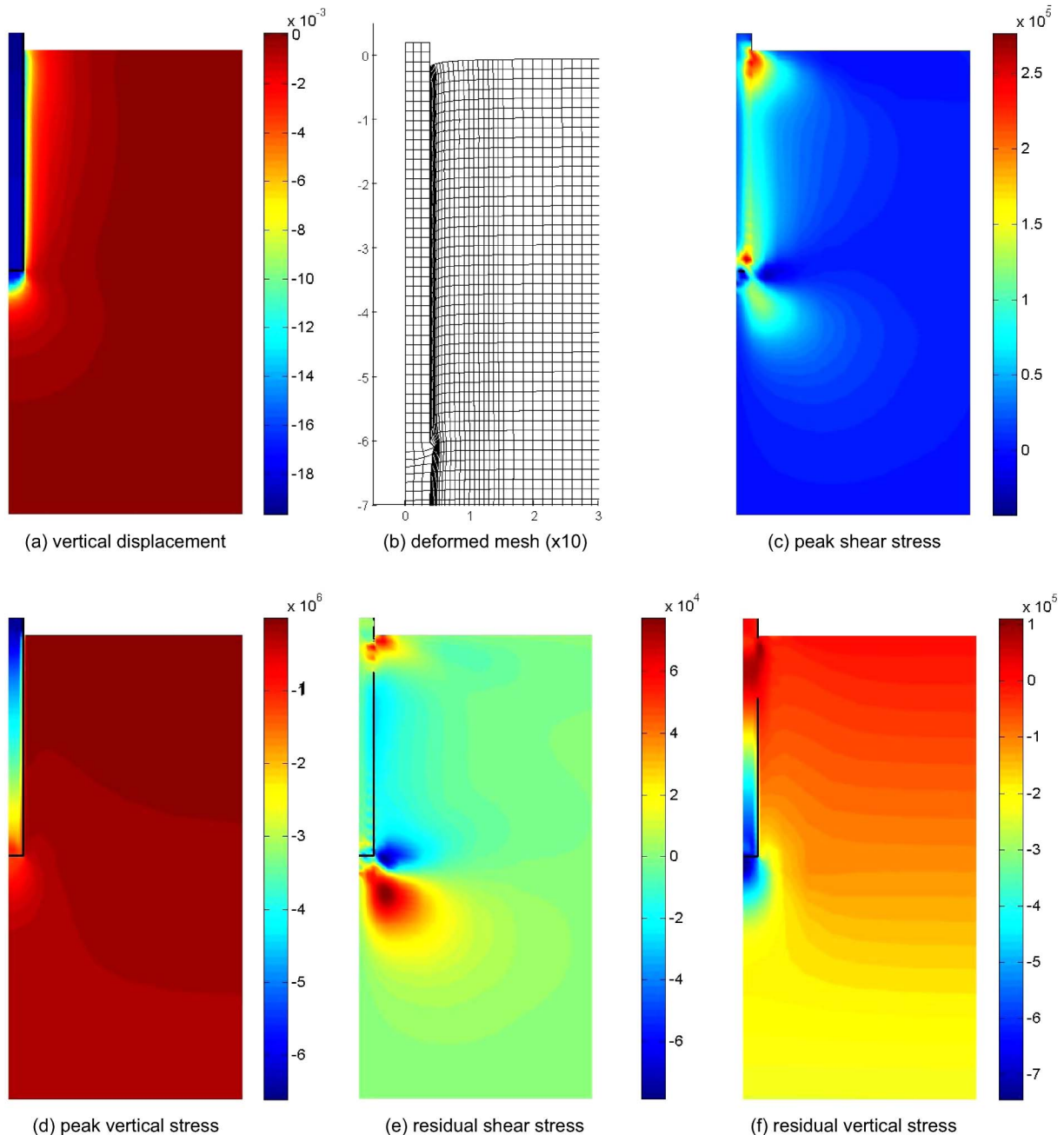

(a) vertical displacement   (b) deformed mesh (x10)   (c) peak shear stress

(d) peak vertical stress   (e) residual shear stress   (f) residual vertical stress

Fig. 11. Computed displacement and stress fields (only showing a subdomain of 6 m long, 12 m deep; unit of stresses in Pa)
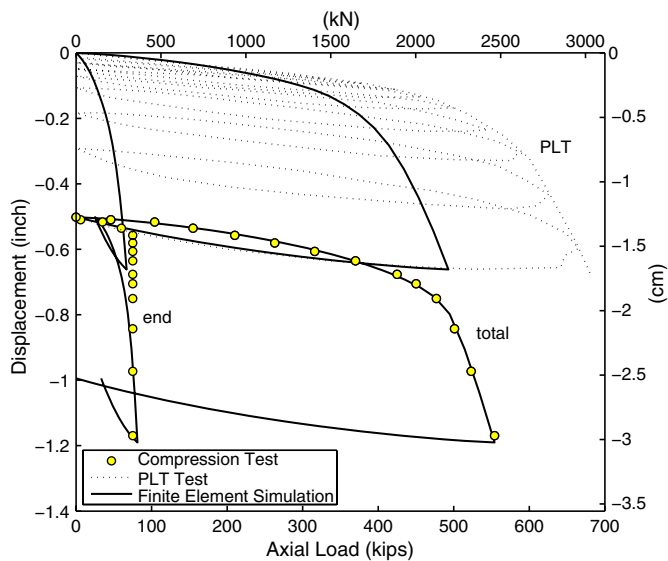
Fig. 12. Finite-element simulation of the static compression test on Pier A1-19

Fig. 13. Computed compressive load distribution on Pier A1-19

to the maximum value, mapping back in the opposite direction afterward. The unloading point in the element corresponds to the point of maximum displacement (i.e., where the strain increment changes direction) but not the applied peak load point. The plastic states during the whole analysis are also monitored, in which 0 stands for the current stress moving inside the bounding surface; 1 for a full plastic state on the bounding surface; and 2 for the stress state moving from the interior onto the bounding surface. The time history of the plastic state indicates that the full plastic stage was reached in the element starting from the second load cycle, in which the shear modulus decreased to a residual value. To measure the intensity of the strain developed within the element, L_2 norm ($\|\varepsilon\| = \sqrt{\varepsilon : \varepsilon}$) was also plotted. The strain level experienced in the element ranges from very small ($10^{-6}\%$) to relatively large (up to 1.3%) under the cyclic loading.

The displacement and stress fields at the peak load point of the last cycle of loading are plotted in Fig. 11. In view of the vertical displacement, the pier as a whole penetrates into the soil. Underneath the pier end, a conical soil wedge is formed and moves together with the pier, with a slip line of approximately 45° inclination [Fig. 11(a)]. Significant displacement and shear stress gradients are localized within one pier radius distance in the soil, [Figs. 11(a) and 11(b)]. Although no special interface element was used in this model, the resolution of strain localization is sharp. The deformed mesh (magnified by a factor of 10) at the peak load is shown in Fig. 11(b). Although the displacement gradient is highly concentrated close to the shaft, the maximum shear strain developed in these elements reaches only approximately 1–3% for all case analyses performed. Therefore, the small deformation assumption that was used in the bounding-surface plasticity theory is still valid. Correspondingly, the secant shear modulus degrades to approximately 5–10% of its maximum value.

The residual displacement and stress fields after the PLT are illustrated in Figs. 11(e) and 11(f). On removal of the applied load on the pier head, approximately 10% of the peak vertical stress is locked beneath the pier end, and the residual shear stress is also concentrated in that area.

The static compression test was performed on Pier A1-19 after the PLT. Because of this, the PLT load history (i.e., the influence of residual displacement and stress condition) had to be properly taken
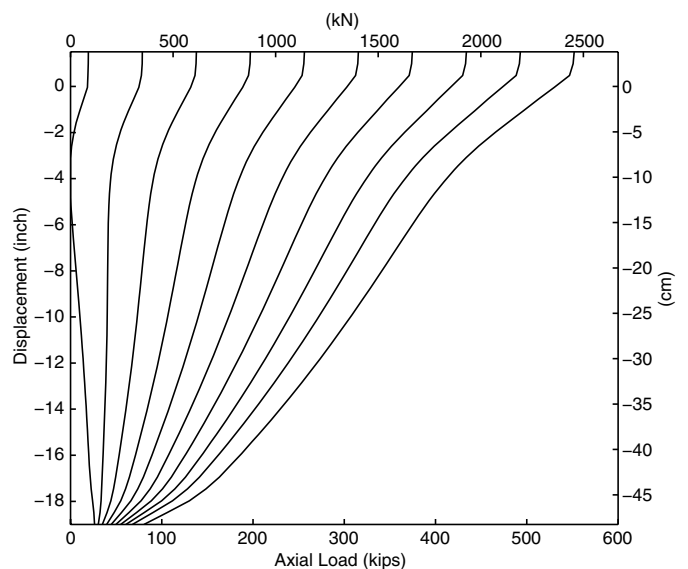
into account in the subsequent static analysis. In the static analysis, the pier was first loaded and unloaded to generate the desired residual displacement. The pier was then loaded again, and the prediction was compared with the measured data. Fig. 12 presents the simulated pier head load-displacement response using the static soil properties in Table 2. The prediction matches the test data very well for both total response and end-bearing components. The compressive load distribution in the pier can also be calculated through integration of stresses over Gaussian points, as shown in Fig. 13. The slope of the distribution curve corresponds to the shear stress of the soil mobilized along the shaft.

The capacity of the proposed model and numerical algorithm has been tested to model other PLTs conducted on piers with different setups and configurations. As in the previous case, the numerical model results agree well with the test data.

Conclusions

A nonlinear finite-element model that successfully captures the nonlinear interaction of the soil-drilled pier system has been developed. The constitutive soil model is based on multiaxial cyclic bounding-surface plasticity, and it is implemented within the general finite-element framework of OpenSees software. The model has been used to model a series of static and dynamic axial load tests on a set of prototype drilled piers, tested as a part of an evaluation of foundation conditions at a site on the University of California, Berkeley campus. The model has shown excellent capability for predicting the stiffness, capacity, and energy-dissipation characteristics of the soil-pier system under both dynamic and static loading conditions. The developed code is quite efficient and suitable for three-dimensional applications.

However, although the present bounding-surface model can reasonably capture system nonlinearity, the stiffness and strength degradation caused by full stress reversal is absent in constitutive formulation. This feature can be important for system prediction in the case of extreme loading conditions. A damage material model should be properly incorporated into current bounding-surface theory to extend the model capacity; for example, the scheme proposed by Allotey and El Naggar (2006) could be considered to address cyclic degradation in a total stress analysis. Significant pore

pressure buildup during earthquake excitation is often experienced, especially in liquefiable ground. The use of an effective stress model could overcome this problem and enhance the model capacity in the future.

Acknowledgments

References

Allotey, N., and El Naggar, H. (2006). "Cyclic degradation/hardening models in total stress analysis: New equations (Paper No. 1015)." *First European Conference on Earthquake Engineering and Seismology*, Swiss Society for Earthquake Engineering and Structural Dynamics, Zurich, Switzerland.

Bathe, K. J. (1996). *Finite element procedures*, Prentice Hall, Upper Saddle River, NJ.

Borja, R. I., and Amies, A. P. (1994). "Multiaxial cyclic plasticity model." *J. Geotech. Eng.*, 120(6), 1051–1070.

Borja, R. I., Chao, H., Montans, F. J., and Lin, C. H. (1999a). "Nonlinear ground response at Lotung LSST site." *J. Geotech. Geoenviron. Eng.*, 125(3), 187–197.

Borja, R. I., Chao, H., Montans, F. J., and Lin, C. H. (1999b). "SSI effects on ground motion at Lotung LSST site." *J. Geotech. Geoenviron. Eng.*, 125(9), 760–770.

Borja, R. I., Lin, C. H., Sama, K. M., and Masada, G. M. (2000) "Modelling non-linear ground response of non-liquefiable soils." *Earthquake Eng. Struct. Dyn.*, 29(1), 63–83.

Borja, R. I., and Wu, W. H. (1994). "Vibration of foundation on incompressible soils with no elastic region." *J. Geotech. Eng.*, 120(9), 1570–1592.

Deeks, A. J., and Randolph, M. F. (1994). "Axisymmetric time-domain transmitting boundaries." *J. Eng. Mech.*, 120(1), 25–42.

Elgamal, A., Yang, Z. H., and Parra, E. (2002). "Computational modeling of cyclic mobility and post-liquefaction site response." *Soil Dyn. Earthquake Eng.*, 22(4), 259–271.

Elgamal, A., Yang, Z. H., Parra, E., and Ragheb, A. (2003). "Modeling of cyclic mobility in saturated cohesionless soils." *Int. J. Plast.*, 19(6), 883–905.

Hughes, T. J. R. (1987). *The finite element method: Linear static and dynamic finite element analysis*, Prentice Hall, Upper Saddle River, NJ.

LoPresti, D. C. F., Jamiolkowski, M., Pallara, O., and Cavallaro, A. (1996). "Rate and creep effect on the stiffness of soils." *Geotechnical special publication*, 61, ASCE, Reston, VA, 166–180.

Lysmer, J., and Kuhlemeyer, R. L. (1969). "Finite dynamic model for infinite media." *J. Engrg. Mech. Div.*, 95(4), 859–877.

Matešić, L., and Vucetic, M. (2003). "Strain-rate effect on soil secant shear modulus at small cyclic strains." *J. Geotech. Geoenviron. Eng.*, 129(6), 536–549.

OpenSees Version 2.3.2 [Computer software]. Pacific Earthquake Engineering Research (PEER) Center, Berkeley, CA.

Prevost, J. H. (1977). "Mathematical modelling of monotonic and cyclic undrained clay behaviour." *Int. J. Numer. Anal. Meth. Geomech.*, 1(2), 195–216.

Prevost, J. H. (1985). "A simple plasticity theory for frictional cohesionless soil." *Soil Dyn. Earthquake Eng.*, 4(1), 9–17.

Rodriguez-Marek, A. (2000). "Near-fault seismic site response." Ph.D. thesis, Univ. of California, Berkeley.

Seed, H. B., Wong, R. T., Idriss, I. M., and Tokimatsu, K. (1984). "Moduli and damping factors for dynamic analyses of cohesionless soils." *Technical Rep. UCB/EERC-84/14*, Earthquake Engineering Research Center, Univ. of California, Berkeley.

Shibuya, S., Mitachi, T., Hosomi, A., and Hwang, S. C. (1996). "Strain rate effects on stress-strain behaviour of clay as observed in monotonic and cyclic traxial tests." *Geotechnical special publication*, Vol. 61, ASCE, Reston, VA, 214–227.

Simo, J. C., and Taylor, R. L. (1985). "Consistent tangent operators for rate-independent elastoplasticity." *Comput. Methods Appl. Mech. Eng.*, 48(1), 101–108.

Sun, J. I., Golesorkhi, R., and Seed, H. B. (1988). "Dynamic moduli and damping ratios for cohesive soils." *Technical Rep. UCB/EERC-88/15*, Earthquake Engineering Research Center, Univ. of California, Berkeley.

Vucetic, M., and Dobry, R. (1991). "Effect of soil plasticity on cyclic response." *J. Geotech. Engrg. Div.*, 117(1), 89–107.

Vucetic, M., Lanzo, G., and Doroudian, M. (1998a). "Damping at small strains in cyclic simple shear test." *J. Geotech. Geoenviron. Eng.*, 124(7), 585–593.

Vucetic, M., Lanzo, G., and Doroudian, M. (1998b). "Effect of the shape of cyclic loading on damping ratio at small strains." *Soils Found.*, 38(1), 111–120.

Vucetic, M., and Tabata, K. (2003). "Influence of soil type on the effect of strain rate on small-strain cyclic shear modulus." *Soils Found.*, 43(5), 161–173.

Wang, G., Kasali, G., and Sitar, N. (2011). "Static and dynamic axial response of drilled piers. I: Field tests." *J. Geotech. Geoenviron. Eng.*, 137(12), 1133–1142.

Wang, G., and Sitar, N. (2006). "Nonlinear analysis of a soil-drilled pier system under static and dynamic axial loading." *PEER Rep. 2006/06*, Pacific Earthquake Engineering Research Center (PEER), Univ. of California, Berkeley.

Zienkiewicz, O. C., and Taylor, R. L. (2000). *The finite element method*, 5th Ed., Elsevier, Amsterdam, Netherlands.